Particle filter-based delamination shape prediction in composites subjected to fatigue loading

Tianzhi Li [1], Francesco Cadini [1], Manuel Chiachío [2,3], Juan Chiachío [2,3], Claudio Sbarufatti [1,*]

[1]*Dipartimento di Meccanica*, *Politecnico di Milano*, *Milan*, *Italy*

[2]*Department of Structural Mechanics and Hydraulic Engineering*, *University of Granada*, *Spain*

[3]*Andalusian Research Institute in Data Science and Computational Intelligence, Granada, Spain*

[*]Corresponding author: *claudio.sbarufatti@polimi.it*

Abstract

Modeling generic size features of delamination, like area or length, has long been considered in the literature for damage prognosis in composites through specific models describing damage state evolution with load cycles or time. However, the delamination shape has never been considered, despite that it holds important information for damage diagnosis and prognosis, including the delamination area, its center, and perimeter, useful for structural safety evaluation. In this context, this paper develops a novel particle filter-based framework for delamination shape prediction. To this end, the delamination image is discretized by a mesh, where control points are defined as intersections between the grid lines and the perimeter of the delamination. A parametric data-driven function maps each point position as a function of the load cycles and is initially fitted on a sample test. Then, a particle filter is independently implemented for each node whereby to predict their future positions along the mesh lines, thus allowing delamination shape progression estimates. The new framework is demonstrated with reference to experimental tests of fatigue delamination growth in composite panels with ultrasonics C-scan monitoring.

Keywords: composite, damage prognosis, particle filter, fatigue delamination, shape prediction

1. Introduction

Composites have been widely used in numerous industries due to their striking benefits such as high strength-to-weight ratio and corrosion resistance, yet they suffer from multiple damage processes, among which fatigue degradation is one of the most common. The degradation initially results in internal damages such as matrix cracking and delamination and eventually brings to fiber, yet catastrophic, failure. In order to timely avoid this issue, inspections are usually required for evaluating the damage state in composites, often resulting in service disruption and therefore high maintenance costs. One desirable scenario for ensuring structural

integrity while keeping maintenance costs at a minimum is to schedule the maintenance just before the damage reaches a critical limit. To this end, an advanced damage prognosis technology is required to provide an anticipated and accurate picture of the future state of damage.

Current damage prognosis practices in composites usually have considered several physics-based damage modes observed during the degradation process, including matrix crack density [1], delamination length or area [2, 3], crack length [4], and stiffness reduction [1, 2, 5, 6], or damage-sensitive statistical features extracted from measured signals, like normalized cumulative energy [7] and cumulative risetime and amplitude [8]. They are based on the fact that damage evolution with load cycles or time under a certain service condition follows a specific pattern, thus the future condition can be calculated by the current state through a proper model depicting such a pattern. From the perspective of the type of information used for modeling the degradation behavior in composites, namely physical knowledge or experimental and in-field data, damage evolution models can be classified either as physics-based [1-5] or data-driven [6-8]. The former ones generally lie within the scope of Paris' law or its extensions, where the rate of damage evolution (e.g., strain energy release rate or stress intensity factor) is analytically calculated [1-3, 5] or fitted from numerical simulations through a data-driven modeling strategy such as Gaussian process [4]. On the other hand, the data-driven approaches, e.g., using neural networks [6] or Markov models [7, 8], resort to sufficient damage data or statistical features extracted from measured signals during the actual degradation process for describing the above relationship.

In practice, the efficiency of any damage evolution model is case-specific, and in general, they provide good results under a number of assumptions [9-11]. However, their capability to account for the uncertainties arising from complex structural degradations, environmental effects, and sensor health conditions is limited [12, 13]. A well-acknowledged strategy to improve their prognostic performance with consideration of the uncertainty is to set the model parameters as unknown state variables to be updated using data by a state estimation technique, such as the particle filter (PF), given its versatility for non-linear and non-Gaussian problems [14-16] and also its demonstrated performance for damage prognosis [2, 3, 17]. The latter implies quantifying the current damage state through a direct or indirect measurement system, depending on whether the damage state can be directly measured or not. More specifically, if a direct measure of the damage is pursued, e.g., by observing the matrix crack density and delamination area through X-ray [1, 2] or the stiffness reduction by strain observations [1, 2], the measurement model will be a simple formulation with the observation equal to the damage state, possibly corrupted by measurement noise. In the case of indirect damage observation, an analytical [4] or data-driven function [3] is required to describe the relationship between the internal damage state and the external observations, for example, relating any local strain [3] or distributed scatter [15] feature to the damage.

Within the referred approaches, delamination prognosis has attracted the attention of the research community due to its threats to structural integrity with invisible warnings [2, 3]. However, delamination shape has never been considered, although it holds important information for damage diagnosis and prognosis, including the delamination area, its center and perimeter, useful for damage growth rate prediction, and finally, structural safety evaluation. Similar to other damage state variables, the progress of delamination shape under a certain loading condition also follows a specific pattern [18], which can be directly observed by X-ray [5] and ultrasonic C-scan [19, 20] or indirectly reconstructed from digital image correlation [20] and guided waves [19, 21].

This paper, therefore, develops a novel particle filter-based delamination shape prediction framework, where C-scan is adopted for delamination imaging. The delamination shape, rather than its area or a specific length, serves as the damage state to be predicted, thus limiting the loss of useful information for prognosis. More specifically, considering the delamination shape is described by some artificially defined control points (CPs), i.e., the intersections between some grid mesh lines and the perimeter of the delamination, the motion of each CP can be modeled with a data-driven parametric function, whose parameters are online updated by a particle filter. The future position of each CP can be located through the updated models and then adopted to reconstruct the future delamination shape. This method is demonstrated with reference to experimental tests of fatigue delamination growth in composite panels with ultrasonics C-scan monitoring.

The rest of this paper is organized as follows: Section 2 gives the methodological details of the proposed framework, including the mesh discretization, the evolution model, and the PF framework for damage shape prediction. The validation of the proposed method by an experiment is given in Section 3. Finally, Section 4 concludes this paper with some topics for future work.

2. Delamination shape prediction

The proposed framework consists of four main steps, namely, (i) defining the mesh nodes and lines for discretizing the delamination shape, (ii) modeling the evolution for each node, (iii) independently updating the evolution parameters of each model through PF, and (iv) calculating the future delamination shape.

2.1 Delamination shape discretization

This study assumes that a delamination image is available through a C-scan monitoring system, or similar technique, as presented in Figure 1 (a). Figure 1 (b) shows the image segmented by some grid lines, whose layout, i.e., the locations of the eighteen cross markers, is kept constant during delamination evolution. Note that a number of control points (CPs) are located where the grid lines intersect the delamination perimeter,

whereas one control length (CL) is taken as the distance between one CP and one corresponding cross marker, e.g., CP4, CP14, CL4, and CL14 in Figure 1 (c).

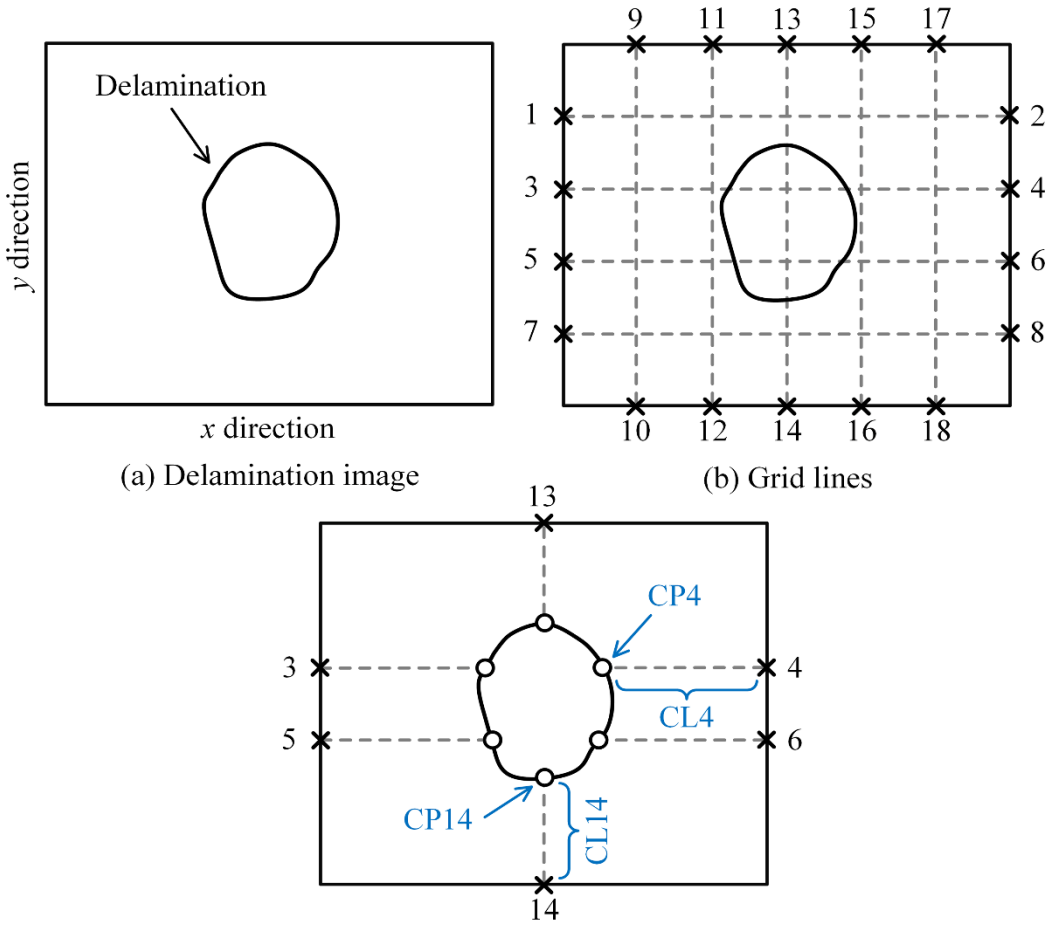

(a) Delamination image (b) Grid lines

(c) Control points (CPs) and control lengths (CLs)

Figure 1 Definition of control points (CPs) and control lengths (CLs) in a delamination image

Since the delamination shape in composites under fatigue loading can grow with a specific pattern [18], the motion of each CP along its corresponding grid line, namely the evolution of each CL, is assumed to follow a certain law, as will be validated in Section 3.2. In this context, the delamination shape prediction problem is reduced to the predictions of these CLs, thus requiring a proper model to describe the evolution of each CL, as well as a state estimation technique to update the model parameters for predicting the future states. Note that, during damage progression, the delamination perimeter will intersect more and more mesh lines, thus increasing the number of CLs and, thus, their relative evolution models. Note that, in this preliminary application, each model is independently updated, under the assumption of the independent evolution of each CL. However, the method could be extended to consider the correlation among CLs' evolutions, which is a matter of future research by the authors.

2.2 Definition of evolution models

Let us assume the evolution of the *l*-th CL can be modeled as

$$z_{l,k} = f_l(N_k, \boldsymbol{\theta}_l) \tag{1}$$

where the subscript *k* means the *k*-th time step, z_l is the control length, N_k is the difference in the number of load cycles between the step of the CL occurrence (zero for all CLs in this study) and the time step *k*, $f_l(\cdot)$ is a data-driven function governing the length evolution with the number of load cycles, and $\boldsymbol{\theta}_l$ is a vector of model parameters.

Given the uncertainties in the delamination growth, the parameters $\boldsymbol{\theta}_l$ are assumed to vary in different specimens of the same structure, and they should be taken as uncertain components to be added in the state vector for online updating, based on a state-space model including the process and measurement equations, as follows:

$$\begin{cases} \boldsymbol{\theta}_{l,k} = \boldsymbol{\theta}_{l,k-1} + \boldsymbol{\omega}_{l,k} \\ z_{l,k} = f_l\left(N_k, \boldsymbol{\theta}_{l,k}\right) + \nu_{l,k} \end{cases} \tag{2}$$

In the last equations, $\boldsymbol{\omega}$ and ν are the process and measurement noises, respectively. Note that the state space model for other CL is the same formulated as above, thus the amount of models utilized for shape prediction at *k*-th step equals that of CLs that are active at that step. Each model will be embedded into an online PF-based scheme due to the assumption of the independent evolution for each CL.

This choice of the state-space, which, as already stated, is also driven by the lack of reliable physics-based descriptions of the delamination shape evolution in composite materials, intuitively allows estimating the parameters of a fitting curve describing the progression of the shape with the number of load cycles. Then, at a given load cycle, the most updated estimates of those parameters (in the form of a particle swarm) are used to project the future CLs, and finally to reconstruct the future delamination shape. The use of a particle filter allows casting this problem into a sequential Bayesian parameter estimation framework, very convenient for online, real-time applications. At the same time, the use of a zero-mean random walk as artificial dynamics for the augmented states representing the possibly constant parameters allows for a certain degree of adaptability of the filter with respect to both training on delamination dynamics different from the current one and sudden changes in the progression behavior, as shown for example in some works by some of the same authors [22, 23].

To be a little more specific, uncertainties (or unknowns) from multiple sources like undetected flaws and environmental effects usually result in different fatigue delamination growths (or more generally, different state evolutions), as shown by the three specimens later. Most uncertainties can hardly be directly embedded into a model, for example, we can hardly find a model with a parameter describing an undetected flaw included. As also described above, the effects of uncertainties on damage growth (or state evolution) are then addressed automatically in the particle filter framework by online updating the parameters of the damage growth (or state evolution) model, as validated in many other damage prognosis investigations, e.g., in [22, 23].

2.3 Particle filter-based model updating

Following a Bayesian approach, the unknown state vector at *k*-th step $\boldsymbol{\theta}_{l,k}$ can be inferred from the measurement, as follows:

$$p(\boldsymbol{\theta}_{l,k}|\boldsymbol{z}_{l,1:k-1}) = \int p(\boldsymbol{\theta}_{l,k}|\boldsymbol{\theta}_{l,k-1}) p(\boldsymbol{\theta}_{l,k-1}|\boldsymbol{z}_{l,1:k-1}) d\boldsymbol{\theta}_{l,k-1} \tag{3}$$

$$p(\boldsymbol{\theta}_{l,k}|\boldsymbol{z}_{l,1:k}) \propto p(z_{l,k}|\boldsymbol{\theta}_{l,k}) p(\boldsymbol{\theta}_{l,k}|\boldsymbol{z}_{l,1:k-1}) \tag{4}$$

where $\boldsymbol{z}_{l,1:k}$ are the measurements collected from time step 1 to *k*, the terms $p(\boldsymbol{\theta}_{l,k}|\boldsymbol{\theta}_{l,k-1})$ and $p(z_{l,k}|\boldsymbol{\theta}_{l,k})$ stands for the transition distribution and the likelihood function, which are driven by the process and measurement equations, respectively, and finally $p(\boldsymbol{\theta}_{l,k}|\boldsymbol{z}_{l,1:k-1})$ and $p(\boldsymbol{\theta}_{l,k}|\boldsymbol{z}_{l,1:k})$ are the prior and posterior probability distribution functions, respectively.

Equations (3) and (4) form the basis for the optimal Bayesian solution, which is rarely possible to be analytically calculated in a nonlinear and non-Gaussian system. Therefore, the sampling importance resampling (SIR) PF [24, 25] is used in this study as an efficient and general state estimation technique. Table 1 lists a pseudo-code implementation of the SIR PF for one CL. Note that, at each time step, a number of PFs equal to the number of active CLs are running in parallel and independently.

Table 1 Sampling importance resampling particle filter for one CL

Initialization: draw N_p particles $\{\boldsymbol{\theta}_{l,0}^i : i = 1,2,\dots,N_p\}$ from the initial distribution $p(\boldsymbol{\theta}_{l,0})$
For *k*=1, 2, …,
Prediction in PF: draw N_p particles $\{\boldsymbol{\theta}_{l,k}^i : i = 1,2,\dots,N_p\}$ by $\boldsymbol{\theta}_{l,k}^i \sim p(\boldsymbol{\theta}_{l,k}|\boldsymbol{\theta}_{l,k-1}^i)$
Weight update: calculate the weight w_k^i by $w_k^i \propto p(z_{l,k}|\boldsymbol{\theta}_{l,k}^i)$, and assign its normalized form $\tilde{w}_k^i$ to each particle $\boldsymbol{\theta}_{l,k}^i$
Resample for $\{\boldsymbol{\theta}_{l,k}^i : i = 1,2,\dots,N_p\}$ using the particle weights $\{\tilde{w}_k^i : i = 1,2,\dots,N_p\}$

Approximate the estimate $\widehat{\boldsymbol{\theta}}_{l,k}$ as $\widehat{\boldsymbol{\theta}}_{l,k} = \frac{1}{N_p}\sum_{i=1}^{N_p} \boldsymbol{\theta}_{l,k}^{i}$

End

2.4 Future delamination shape prediction

The target of this SHM application is that of predicting the future CLs based on the updated PF estimates $\widehat{\boldsymbol{\theta}}_{l,k}$, then locating the future CPs, and finally constructing the future delamination shapes. Thus, by combining the evolution model by Eq. (1) and the *k*-th posterior distribution of its parameters $p\left(\boldsymbol{\theta}_{l,k}\middle|\boldsymbol{z}_{l,1:k}\right)$, the *j*-th step ahead of the *l*-th CL $z_{l,k}^{j}$ can be calculated as in Table 2:

Table 2 Calculation of future *l*-th control length

For $i = 1 : N_p$

For $j = 1, 2, 3, \ldots$

Calculate future $z_{l,k}^{i,j}$ as $z_{l,k}^{i,j} = f_l\left(N_{k+j}, \boldsymbol{\theta}_{l,k}^{i}\right)$

End

End

Figure 2 reveals how this method works for one future step, while the same procedure also applies to all the other future steps. Figure 2 (a) shows the means and 95% confidence boundaries (CBs) of the predicted CL after one step, which can then be used for locating the corresponding CPs, as plotted in Figure 2 (b). By resorting to a curve fitting strategy, i.e., the MATLAB® function 'cscvn', is used in this study, the delamination shape can be constructed by these discrete CPs, as shown in Figure 2 (c). Note that a simple rule will be used to merge these discrete CBs into a global CB for delamination shape: those lying within the mean delamination shape will be adopted for building the lower global CB of delamination shape, while those outside the mean shape are used for upper global CB.

Finally, inspired by the cumulative relative accuracy (CRA) in [26], a new CRA is developed in this study to evaluate the accuracy of the shape predicted at *j*-th ahead step based on the estimates at *k*-th step as,

$$CRA_{k,j} = \frac{1}{N_r}\sum_{q=1}^{N_r}\left(1 - \frac{\left|d_{target}^{k,j,q} - d_{pred}^{k,j,q}\right|}{d_{target}^{k,j,q}}\right) \tag{5}$$

where N_r means the number of reference lines (RLs), each of which is a ray starting at the reference point

(RP, simply defined as the center of the image in this study) with a certain angle α to the x-direction, d_{target} is the distance between the RP and the target shape perimeter along with a specific RL, whereas d_{pred} is the distance between the RP and the predicted shape perimeter, as shown in Figure 2 (d). Note that the CRA indicator should lie in the [-∞,1] interval, where a higher CRA means a more accurate prediction, and vice-versa.

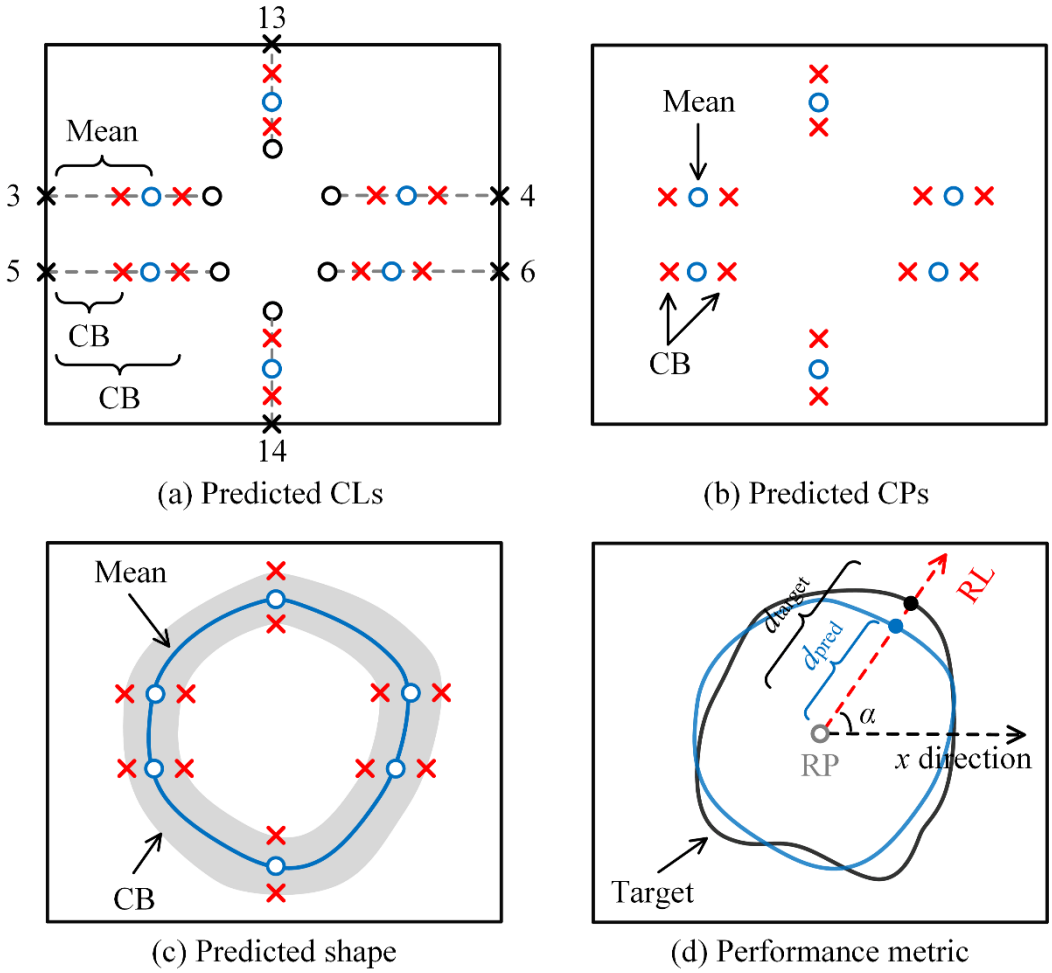

Figure 2 Future shape prediction procedure and performance evaluation
Note: 'CL, 'CP', 'CB', 'RP', and 'RL' means 'control length', 'control point', 'confidence boundary', 'reference point', and 'reference line', respectively.

3. Application

The context of the engineering application of this manuscript is given in this subsection, along with information on the source of the data used and how they have been processed for reproducibility.

3.1 Experimental setup

The proposed framework is applied to fatigue cycling data obtained from a set of run-to-failure fatigue experiments in cross-ply carbon-epoxy laminates. The tests were conducted using a servo-hydraulic

Instron/Schenk® 100 kN tension-tension test machine with hydraulic clamps (see Figure 3(a)). Cycom 977-2-35-12 k HTS pre-impregnated (commonly known as *prepreg*) material was used for rectangular 250 × 35 [mm] coupons with 2 [mm] thickness and $[0/90]_{4S}$ stacking sequence. The coupons were cured in an autoclave at 177 [°C] for 3 [h] using a pressure of 7 [bar]. To induce an initial local state of matrix-cracks and delamination, impact damage was introduced using a semi-spherical striker drop weight tower, which produced 3.8 Joule impact energy. The fatigue tests were carried out at a maximum applied load of 49 [KN], a frequency $f = 6$ [Hz], and a stress ratio $R = 0.1$. Further details about the material properties along with the fatigue test data are given in Table 3.

Table 3 Mechanical and manufacturing parameters of the

Type	**Parameter**	**Value**	**Units**	**Description**
Mechanical	E_m	*3.52*	GPa	*Matrix stiffness*
	ν_m	*0,35*	--	*Poisson's ratio of the matrix*
	E_{fx}	*240*	GPa	*X-axis laminate stiffness*
	E_{fy}	*28*	GPa	*Y-axis laminate stiffness*
	σ_{fx}	*1160*	MPa	*X-axis failure tension*
Manufacturing	v_f	*0.65*	--	*Fiber volume fraction*
	ρ_f	*1770*	Kg/m^3	*Fiber density*

Monitoring data were collected from laser extensometer for online strain measurements, and infrared thermography and C-scan for off-line delamination monitoring, although in this work, only the C-scan data are used for demonstration purposes. C-scan measurements were carried out using a *USPC 3040 DAC* from Ingenieurbüro Dr. Hillger® system (see Figure 3 (b)), with a resolution of 20 [MHz] and amplification of up to 106 [dB] in 0.5 [dB] steps. Figure 3(c) shows a sample C-scan image obtained during the experiments.

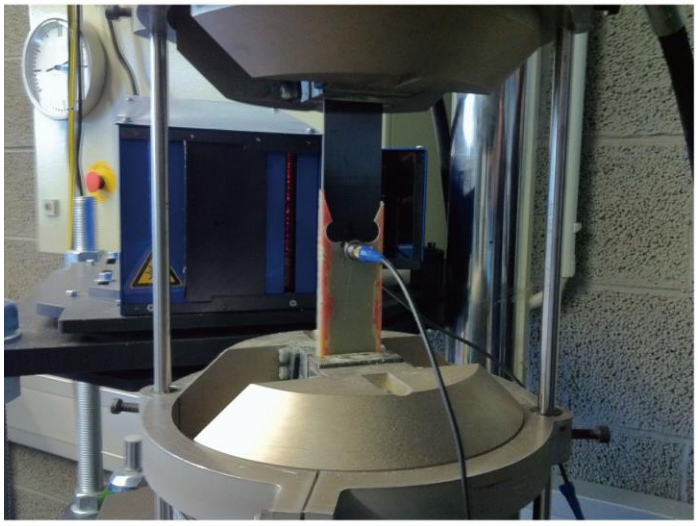

(a) Fatigue test

(b) Ultrasonic C-scan system

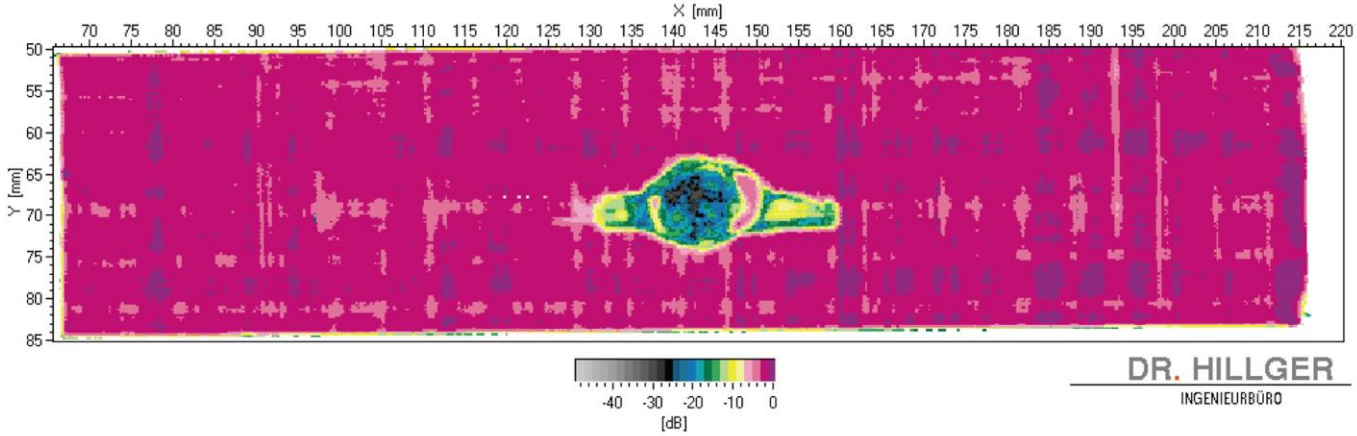

(c) Sample delamination image at 10000 load cycles for specimen S1

Figure 3 Fatigue test for composite panel with ultrasonic c-scan monitoring system

3.2 Image processing

Figure 4 shows the four steps for processing the raw ultrasonic C-scan delamination image to identify the control points (CPs) and control lengths (CLs). They can be taken as a sequence of actions triggered after an alarm is drawn by a damage detection and localization strategy:

(i) Image cropping: a 55 × 15 [mm] rectangle sub-image, centered on the delamination, is extracted from the raw image at each load cycle step. Though specific for the case under analysis, in the most general case, the rectangle dimension can be tuned according to limits on damage sizes imposed by certification authorities or airworthiness.

(ii) Extraction of delamination contour. The dB unit provides a measure of the depth of delamination, such that a lower amplitude means deeper delamination within the laminate thickness. As a generic rule of thumb specific to this application, the contour is selected as the area limit where the signal amplitude is less than -6 dB. Though a visual check is adopted here for better control of the target delamination perimeter, automatic delamination contour identification is possible, leaving the PF the assignment to filter the additional

unavoidable uncertainty.

(iii) Definition of grid lines, using seven grid lines to segment the image, located at the following x - y coordinates: x = 22.5, 27.5, 32.5, and y = 5, 6.5, 8.5, 10, where the units are expressed in [mm].

(iv) Definition of CPs and CLs: the CPs can be defined as the intersections between the grid lines and the delamination contour, whereas the CLs are taken as the distance between the CPs and the corresponding cross-markers.

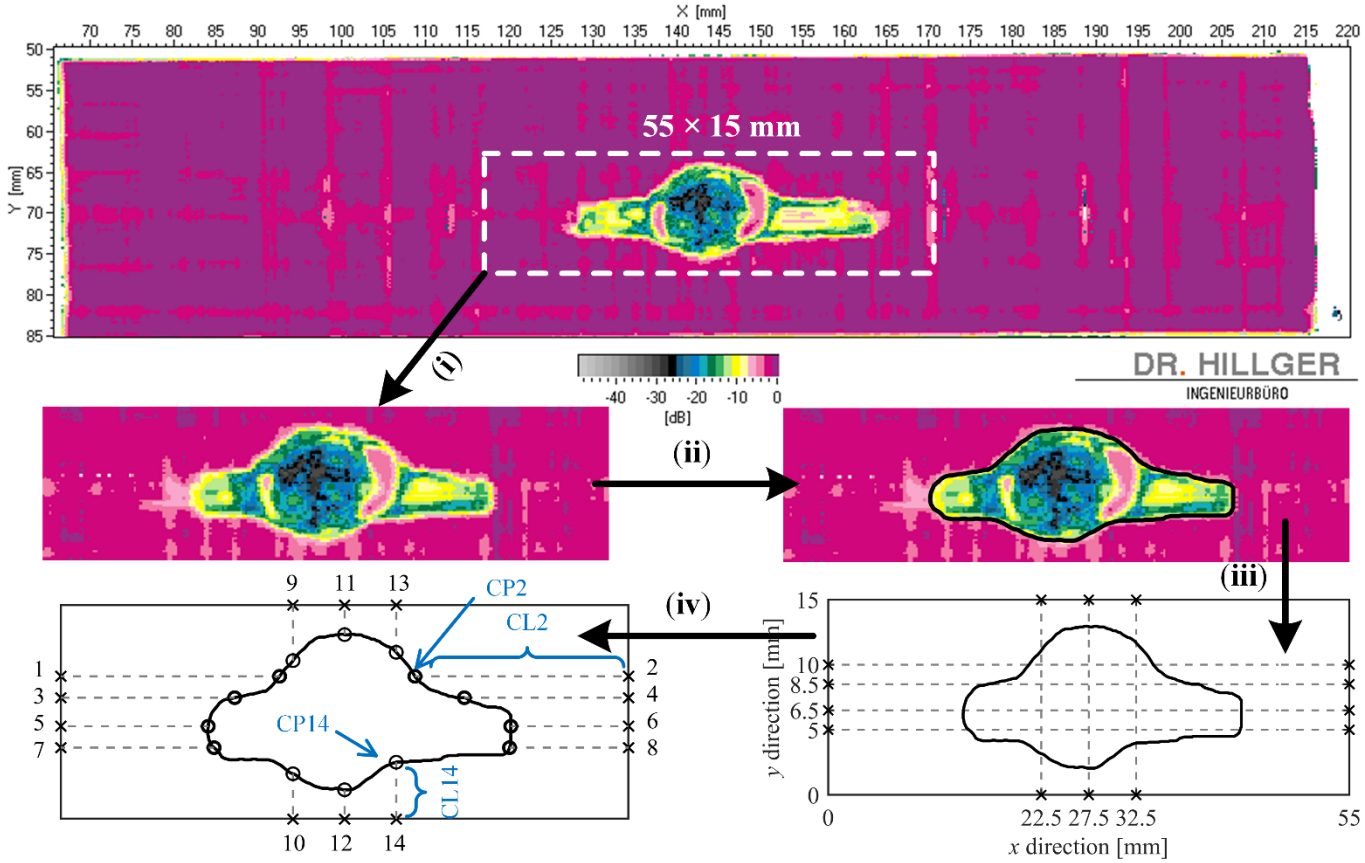

Figure 4 Image processing procedure

The delamination shapes at different load cycles for three specimens S1, S2, and S3 are extracted by Steps (i) and (ii), and they are given in Appendix A.1. Note that for each specimen, the delamination grows under a similar pattern, i.e., it propagates along the x-direction (the load direction) but not along the y-direction. To better understand the damage evolution pattern, Figure 5 shows the growths of four selected CLs from three specimens, where can be observed that both CL12 and CL14 remain stable during the fatigue test, whilst CL4 decreases with load cycles but at different rates. These observations demonstrate that CLs from different specimens can evolve under a similar pattern, and also that a deterministic evolution model can hardly provide an accurate prediction, as already mentioned in [14-16]. The latter is even more evident in Figure 5 (d), where CL8 from specimens S2 and S3 remain stable with load cycle steps, while those from S1 strictly decrease over fatigue cycles.

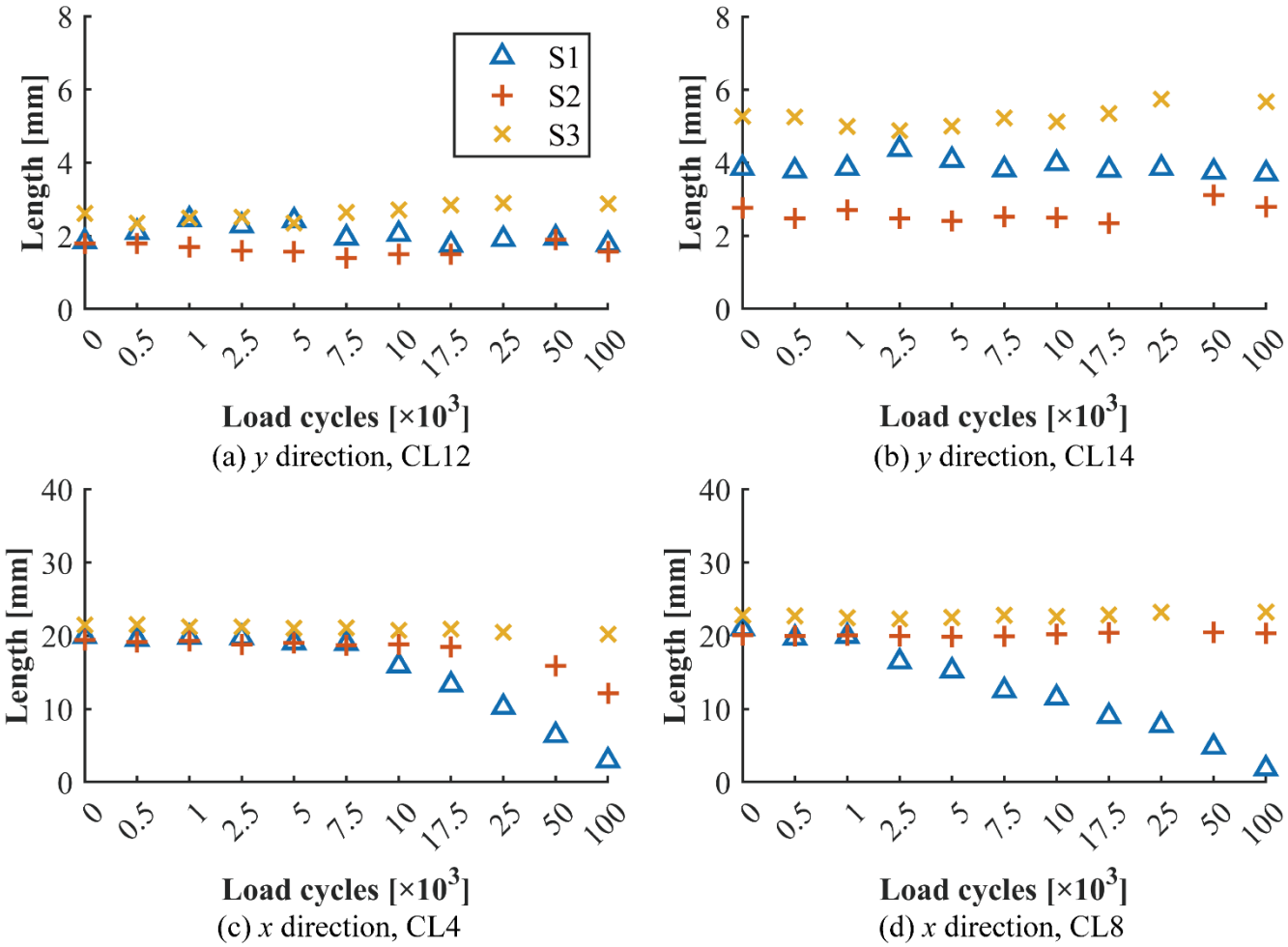

(a) *y* direction, CL12 (b) *y* direction, CL14

(c) *x* direction, CL4 (d) *x* direction, CL8

Figure 5 Growths of selected control lengths from specimens S1 – S3

3.3 Modeling and PF parameters

Given the demonstrated performance of polynomial fitting for depicting fatigue degradation [27, 28], a second-order polynomial function is adopted to map the *l*-th CL and the number of load cycles, as follows

$$z_{l,k} = p_{1,l,k}N_k^2 + p_{2,l,k}N_k + p_{3,l,k} \tag{6}$$

where the polynomial coefficients $p_{1,l}$, $p_{2,l}$ and $p_{3,l}$ are taken as the evolution parameters for the *l*-th CL.

Thus, the state space model for the *l*-th CL can then be formulated as

$$\begin{cases} \begin{bmatrix} p_{1,l,k} \\ p_{2,l,k} \\ p_{3,l,k} \end{bmatrix} = \begin{bmatrix} p_{1,l,k-1} \\ p_{2,l,k-1} \\ p_{3,l,k-1} \end{bmatrix} + \begin{bmatrix} \omega_{1,l,k} \\ \omega_{2,l,k} \\ \omega_{3,l,k} \end{bmatrix} \\ z_{l,k} = p_{1,l,k}N_k^2 + p_{2,l,k}N_k + p_{3,l,k} + \nu_{l,k} \end{cases} \tag{7}$$

where $\omega_{1,l}$, $\omega_{2,l}$ and $\omega_{3,l}$ are the process noise, and ν_l is the measurement noise. Additionally, kernel smoothing [29] is adopted to improve the estimation performance for the parameters $p_{1,l}$, $p_{2,l}$ and $p_{3,l}$, as

already used in [3, 16]. Taking the parameter $p_{1,l}$ as one reference example, kernel smoothing can be presented as:

$$p_{1,l,k} = \sqrt{1-h^2}\,p_{1,l,k-1} + \left(1-\sqrt{1-h^2}\right)\hat{p}_{1,l,k-1} + \omega_{1,l,k} \tag{8}$$

where $\hat{p}_{1,l,k-1}$ is the estimate of $p_{1,l,k-1}$, and h is the kernel smoothing parameter. The same procedure applies to the other two parameters $p_{2,l}$ and $p_{3,l}$.

Next, the model for each l-th CL is updated within an independent PF whose hyperparameters have been selected through a trial-and-error procedure, as reported in Table 4. More details on the effects of these parameters on the estimate and confidence boundary can be found in literature, as for the number of particles [30], the standard deviation (STD) in the likelihood function [3], the kernel smoothing parameter [3], the initial ranges [30], and the process noise [3, 30], while some comments are provided hereafter as for the selection of the initial ranges of model parameters.

Table 4 Particle filter parameters for the l-th control length

Number of particles N_p	STD in likelihood function σ_y	Kernel smoothing parameter h
6000	0.4	0.2
Initial ranges for $\{p_{1,l}, p_{2,l}, p_{3,l}\}$		
$p_{1,l,0}\sim \mathrm{U}(m_{1,l}-r_{1,l}, m_{1,l}+r_{1,l})$	$p_{2,l,0}\sim \mathrm{U}(m_{2,l}-r_{2,l}, m_{2,l}+r_{2,l})$	$p_{3,l,0}\sim \mathrm{U}(m_{3,l}-r_{3,l}, m_{3,l}+r_{3,l})$
Distributions of process noises $\{\omega_{1,l}, \omega_{2,l}, \omega_{3,l}\}$ for $\{p_{1,l}, p_{2,l}, p_{3,l}\}$		
$\omega_{1,l}\sim \mathcal{N}(0, (1\times 10^{-12})^2)$	$\omega_{2,l}\sim \mathcal{N}(0, (1\times 10^{-7})^2)$	$\omega_{3,l}\sim \mathcal{N}(0, 1^2)$

Note: (a) $\{m_1, m_2, m_3\}$ and $\{r_1, r_2, r_3\}$ are the PF parameters for defining the initial ranges; (b) the terms $\mathrm{U}(\cdot)$ and $\mathcal{N}(\cdot)$ indicate uniform distribution and Gaussian probability density function, respectively.

Though one can expect algorithm convergence without informative priors on model parameters, in order to limit the number of particles and to facilitate convergence to target parameters, we tested a scenario in which all the delamination images from two specimens are used to "train" the initial ranges of state parameters, while those from a third specimen are taken as the testing case. More specifically, results for training with S2 and S3 and testing on S1 are shown in Section 3.4, while discussion on other combinations is provided in Section 3.5.

A general belief for this kind of problem is that 'the predictions will be more accurate with an

increasing number of images (or CLs) used for initialization until the number of images becomes large enough'. For different applications (or different specimens in the same application, or even different numbers of load cycles for the same specimen), the definition of 'enough' should probably be different, and it can hardly be calculated online. Thus, a general recommendation could be to use the images as much as possible.

In order to use more CLs for "training" the initial ranges of the parameters of each CL evolution model, the fourteen CLs have been classified into four groups based on their expected similarity, as listed in Table 5. For each group, the centers $\{m_1, m_2, m_3\}$ for the initialization ranges are defined as the mean parameters providing the best fitting on the initialization sets, while $\{r_1, r_2, r_3\}$ (related to the parameter prior uncertainty) are defined through a trial-and-error procedure.

Table 5 Four groups of control lengths

Group	Direction	Control length (CL)	$\{m_1, m_2, m_3\}$	$\{r_1, r_2, r_3\}$
1	x	1, 2, 7 ,8	$\{1.54 \times 10^{-10}, -4.42 \times 10^{-5}, 20.9\}$	$\{4 \times 10^{-10}, 4 \times 10^{-5}, 4\}$
2	x	3, 4, 5, 6	$\{0.44 \times 10^{-10}, -1.93 \times 10^{-5}, 20.2\}$	$\{4 \times 10^{-10}, 4 \times 10^{-5}, 4\}$
3	y	9, 10, 13, 14	$\{-0.82 \times 10^{-10}, 0.12 \times 10^{-5}, 3.67\}$	$\{1 \times 10^{-10}, 1 \times 10^{-5}, 2\}$
4	y	11, 12	$\{-1.29 \times 10^{-10}, 1.57 \times 10^{-5}, 1.87\}$	$\{1 \times 10^{-10}, 1 \times 10^{-5}, 2\}$

3.4 Shape prediction results

Results for prediction of S1 degradation, based on prior knowledge within S2 and S3 degradations, are reported hereafter. Figures 6 (a) and (b) show the parameter estimation results for two CLs along the *y*-direction, i.e., CL12 and CL14, respectively, while Figures 6 (c) and (d) show those for two CLs along the *x*-direction, CL4, and CL8, respectively. In each plot, particles representing samples of the three evolution parameters in Eq. (6), namely p_1, p_2, and p_3, gradually reduce their spread during the estimation process and finally accumulate within certain ranges, demonstrating that PF can provide satisfactory filtering. Noticeably, parameters of the two *x*-direction CLs exhibit larger shifts than those of the two *y*-direction CLs, due to the larger delamination growth along the *x*-direction, as shown in Appendix A1.

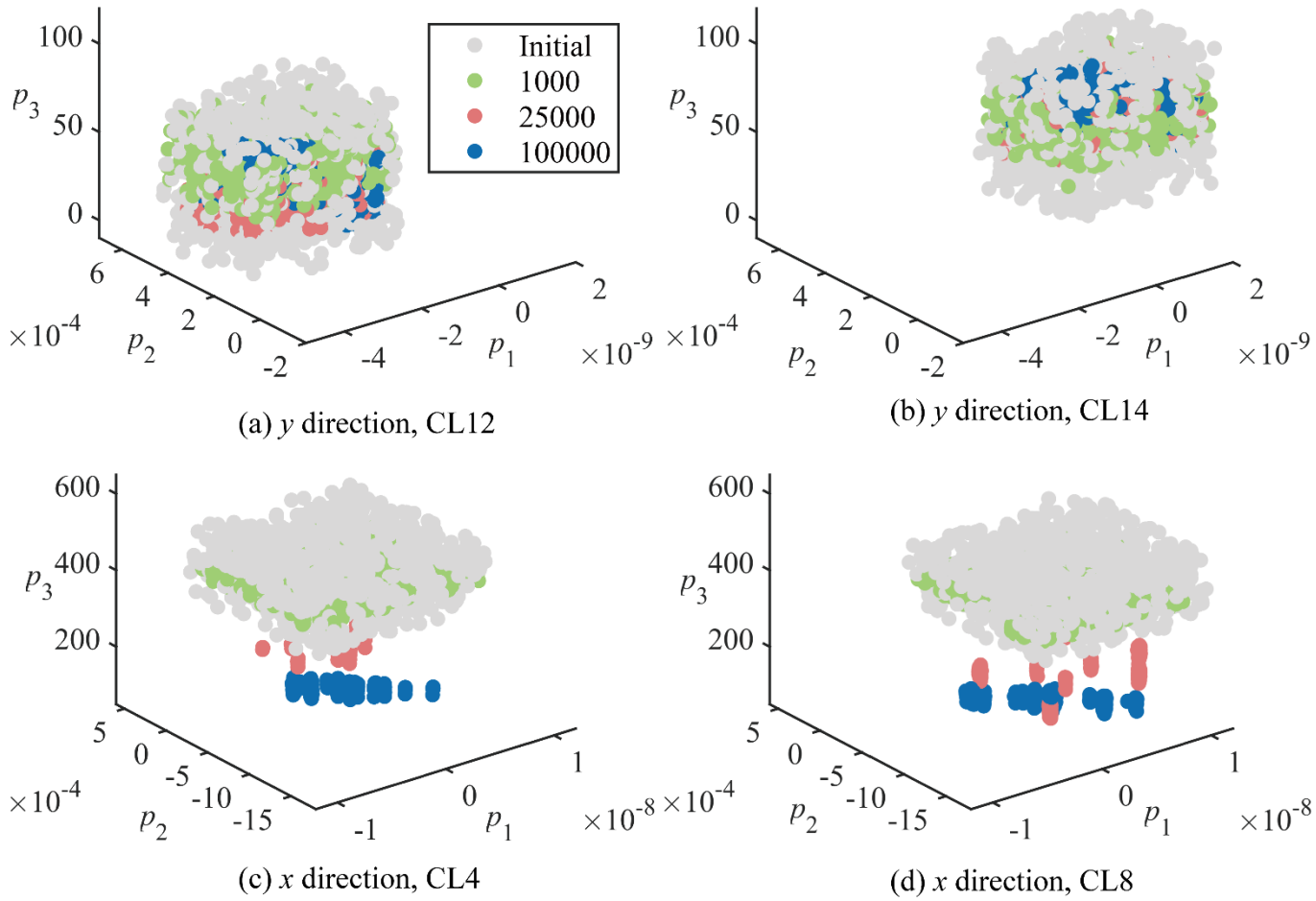

(a) y direction, CL12

(b) y direction, CL14

(c) x direction, CL4

(d) x direction, CL8

Figure 6 Parameter estimation results for four control lengths for specimen S1

Figures 7 (a-b), 7 (c-d), and 7 (e-f) show the predictions for the two y-direction CLs based on their PF parameter estimates at 1000, 10000, and 25000 load cycles, respectively. Note the means of the predictions remain close to the target, and their 95% CBs embrace the target values, proving that the evolution models of the two selected CLs are correctly updated by the PF within a few measurement steps.

Figures 8 (a-b), 8 (c-d), and 8 (e-f) show the predictions for the two x-direction CLs based on their PF parameter estimates at 1000, 10000, and 25000 load cycles, respectively. Predictions overestimate the target lengths at lower cycles, due to the shape bias between specimens S2 and S3 (used for setting the initialization ranges for parameters) and specimen S1 (used for testing). However, the predictions of the two x-direction CLs become more accurate as more delamination images are processed.

The difference in the prediction performances of the CLs along the x and y directions is actually due to the adaptation speed of the filter, rather than to the fact that the artificial dynamics are used for the polynomial form coefficients. In turn, the adaptation speed is related to the number of available measurements (the more, the faster the filter) and also to the CL evolutions available for the initialization. It can be seen, in fact, that the evolutions of the x-direction CLs for specimens S2 and S3 are much slower than those of

specimen S1, so that the filter initially "expects" (and coherently predicts) a slower evolution: unfortunately, the number of observations available is not sufficiently high for the filter to capture the faster dynamics, at least not until the last observations, when it seems to finally converge.

In general, it can be concluded from Figures 6, 7, and 8 that the proposed methodology can provide satisfactory estimates of the evolution model parameters and accurately anticipate the future CL, and thus the delamination shape, after a sufficient number of delamination images is processed for parameter updating.

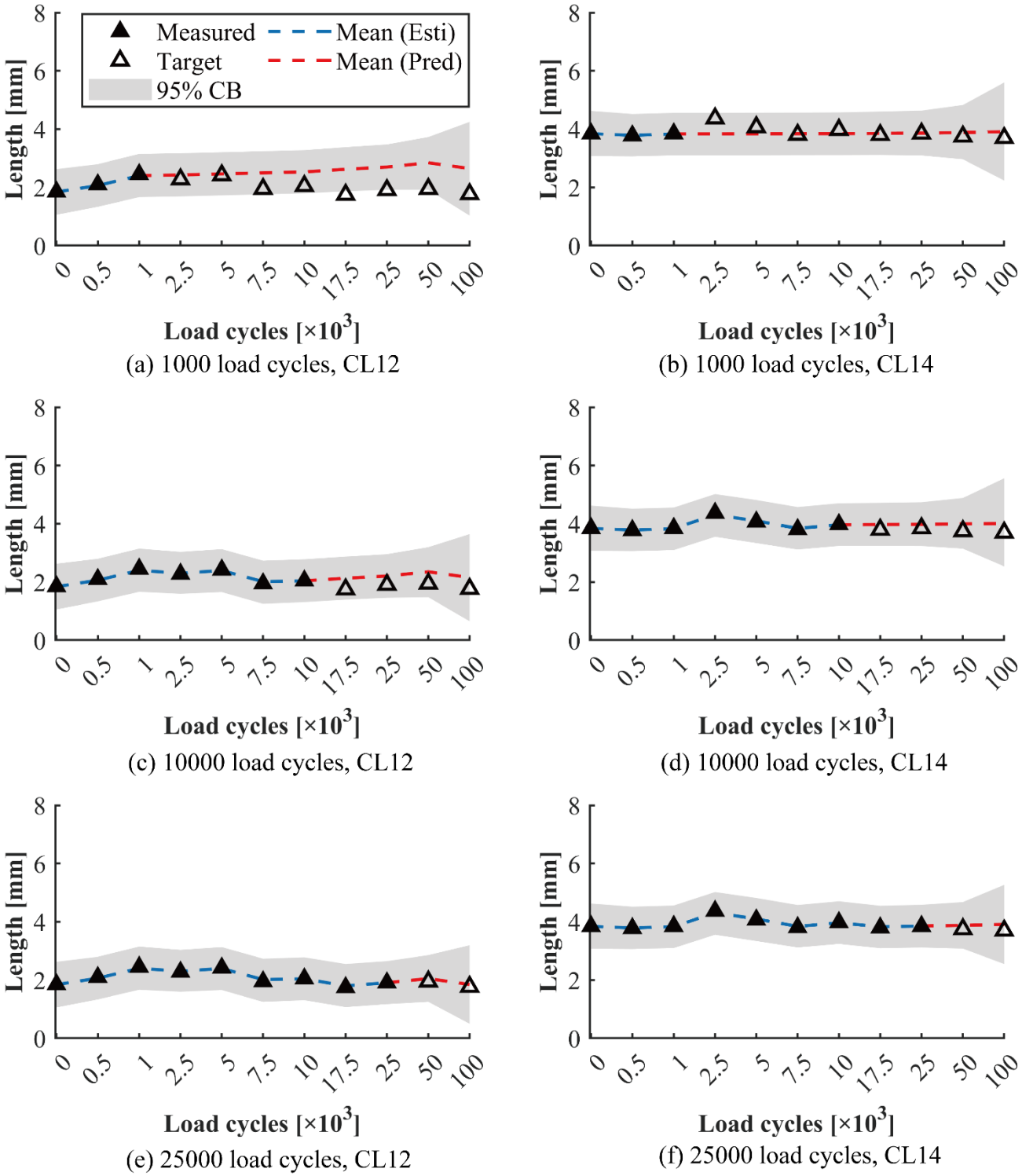

(a) 1000 load cycles, CL12

(b) 1000 load cycles, CL14

(c) 10000 load cycles, CL12

(d) 10000 load cycles, CL14

(e) 25000 load cycles, CL12

(f) 25000 load cycles, CL14

Figure 7 Predictions for two *y*-direction control lengths with the estimates at three selected load cycles for specimen S1

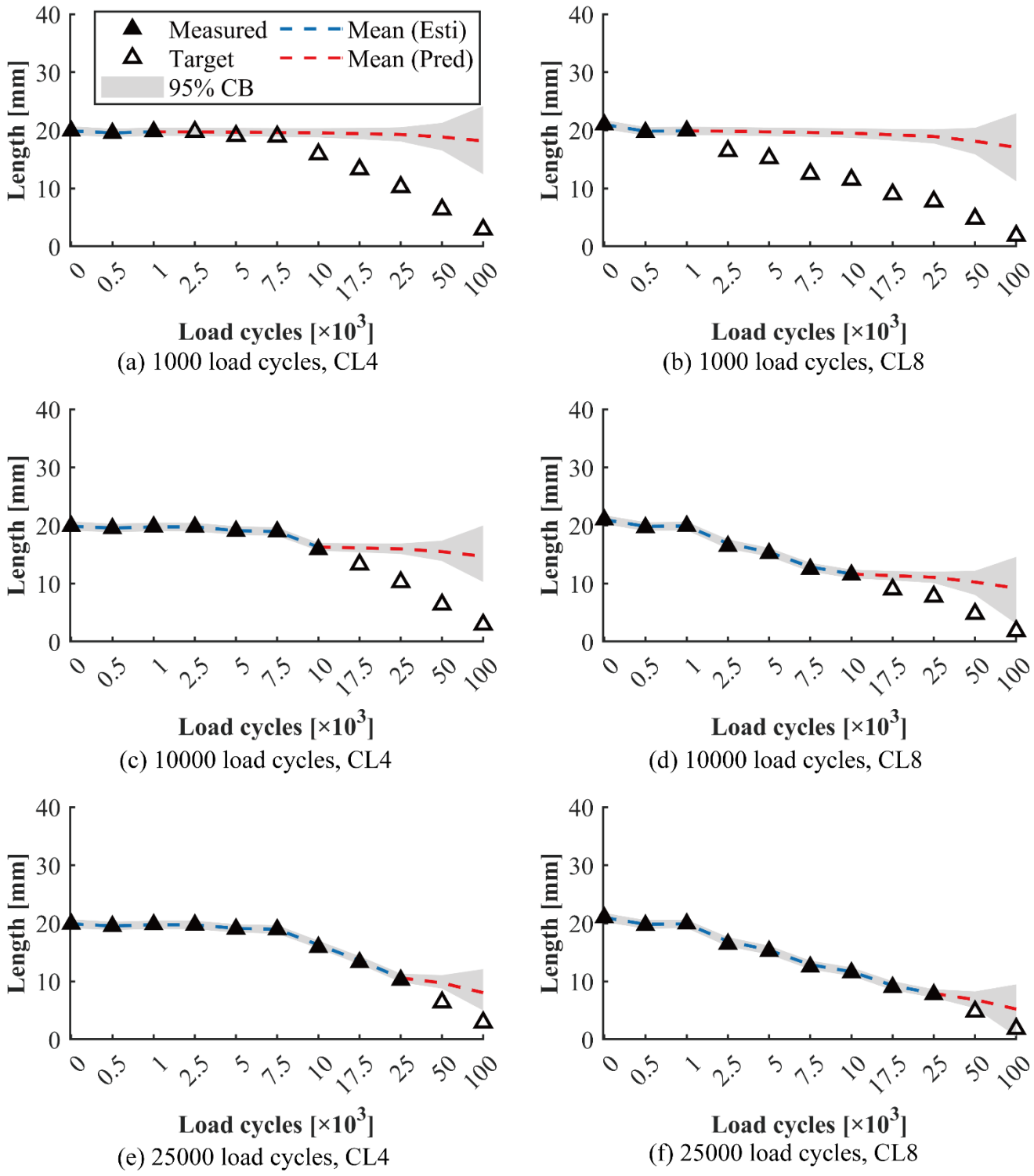

(a) 1000 load cycles, CL4

(b) 1000 load cycles, CL8

(c) 10000 load cycles, CL4

(d) 10000 load cycles, CL8

(e) 25000 load cycles, CL4

(f) 25000 load cycles, CL8

Figure 8 Predictions for two *x*-direction control lengths with the estimates at three selected load cycles for specimen S1

After acquiring the future CLs, the control points (CPs) and their CBs can be located and then used to shape the future delamination, as performed in Section 2.4. For simplicity, only the delamination shape predicted with the estimates at 1000, 10000, and 25000 load cycles are given in Figures 9 (a), (b), and (c), respectively. It can be observed that the shape prediction becomes less accurate while increasing the steps ahead for prediction, as the uncertainties of delamination growth also increase ahead in the future. On the other hand, the prediction at one specific future step gets more accurate if more delamination images are

adopted for model updating, due to the convergence of the evolution parameters as shown in Figure 6.

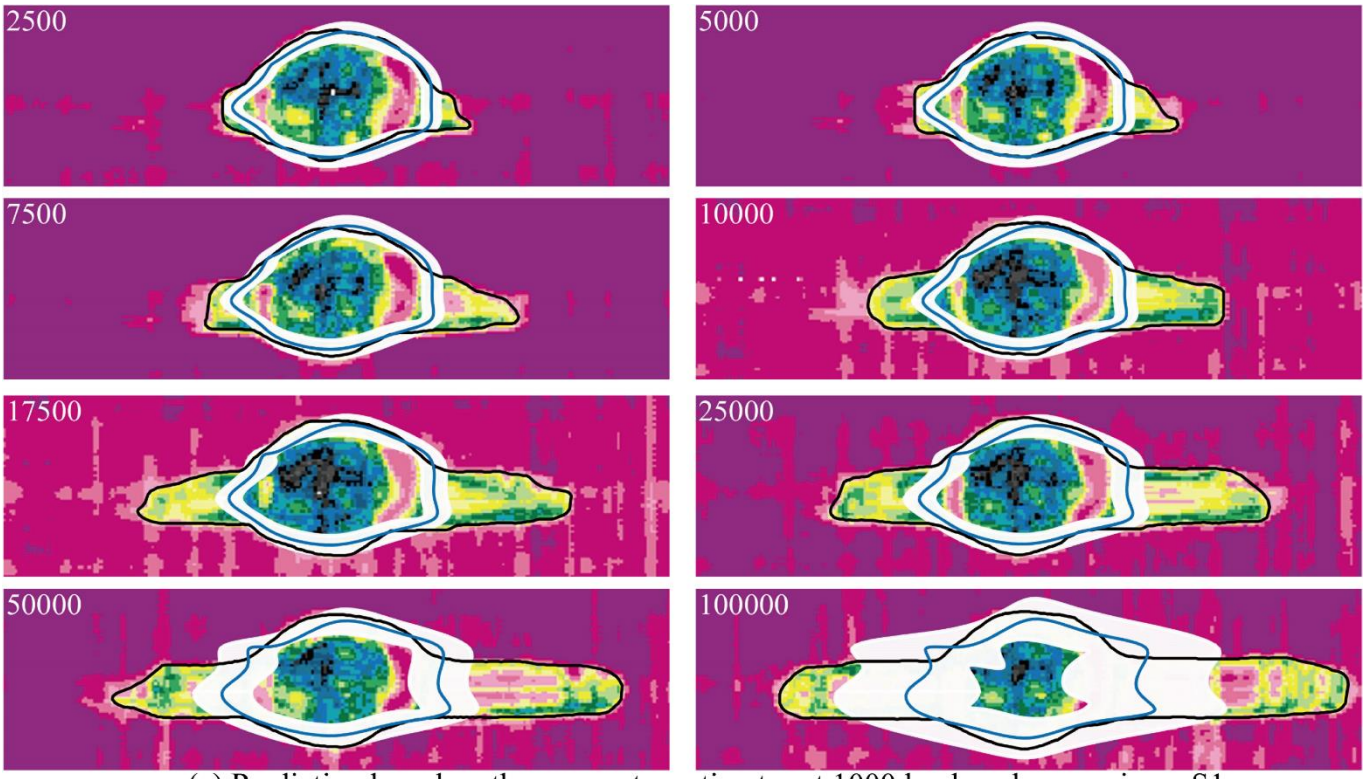

(a) Prediction based on the parameter estimates at 1000 load cycles, specimen S1

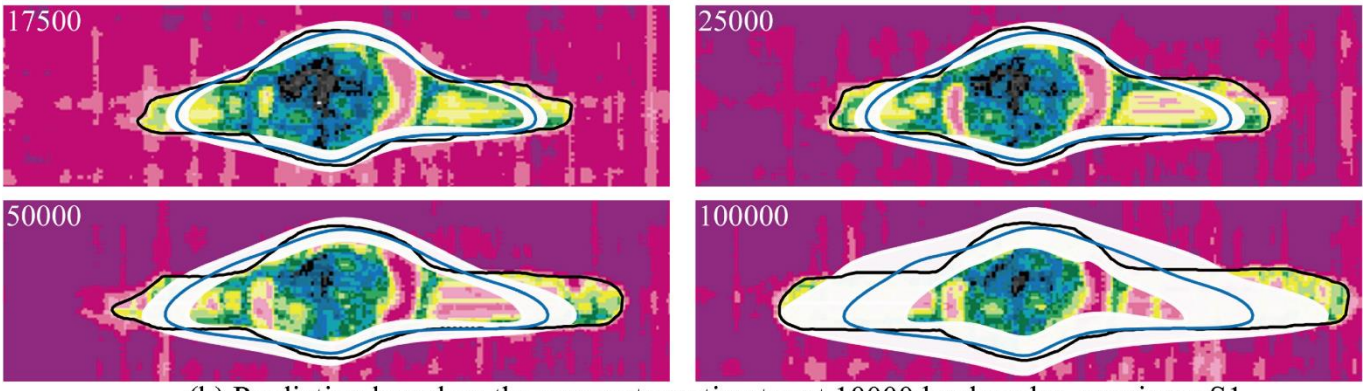

(b) Prediction based on the parameter estimates at 10000 load cycles, specimen S1

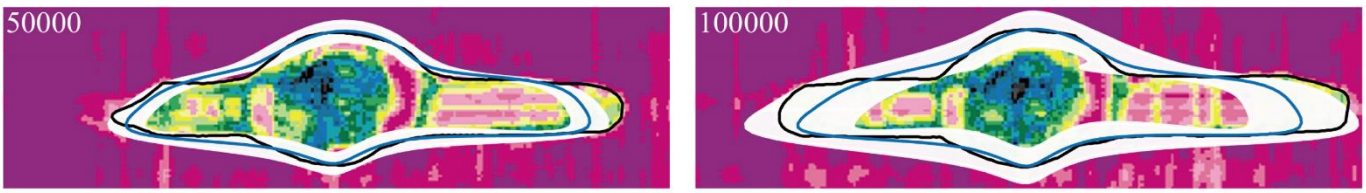

(c) Prediction based on the parameter estimates at 25000 load cycles, specimen S1

Figure 9 Shapes predicted at future load cycles based on the estimates at three selected load cycles for specimen S1

Note: the load cycles at which the future shape is predicted are in the left-top corner. The black curve, blue curve, and white area are the target shape, the predicted shape, and its 95% CBs, respectively.

After defining RF as the center of the delamination image, i.e. [27.5 mm, 7.5 mm] based on the reference system of the s-scan images in Figure 9, and $\boldsymbol{\alpha} = [0, 5, 10, 15, 45, 90, 135, 165, 170, 175, 180, 185, 190, 195, 235, 270, 315, 345, 350, 355]$ degrees with respect to the x-direction, the CRA prognostic performance metric is shown in Figure 10 for different future

load cycles based on the parameter estimates at different steps of delamination growth. The same conclusions drawn after Figure 9 are valid, as highlighted by the red and green arrows.

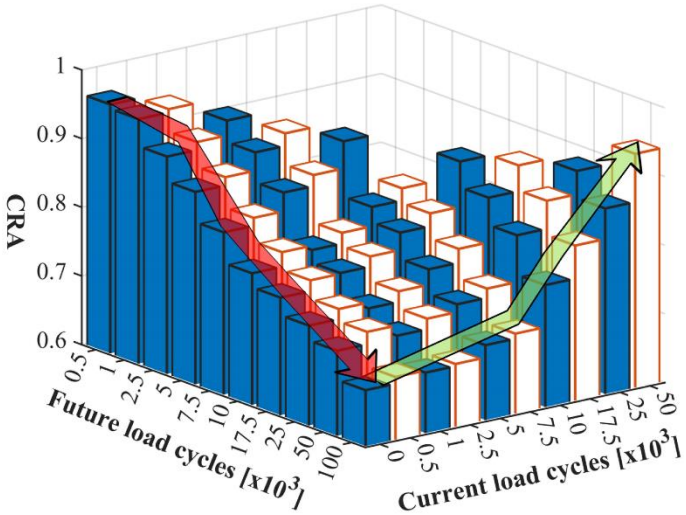

Figure 10 Cumulative relative accuracies (CRAs) of shape predictions for specimen S1

Note that our case study is based on a series of laboratory tests, not focused on studying the effects of variable loading. However, according to our previous experience and the results obtained in some previous works by some of the same authors [22, 23], we can expect that the filters, even if initialized on the basis of different load amplitude, should be able to adapt to the new, changed conditions (provided they are not too different from the initial ones), albeit at the expense of some convergence delays.

3.5 Predictions for other specimens

The proposed framework is also tested for specimens S2 (with parameter initialization based on S1 and S3) and S3 (with parameter initialization based on S1 and S2), while the same procedure as in Section 3.3 is used for the definition of $\{m_1, m_2, m_3\}$. Also, the other PF hyperparameters are the same as those in Section 3.3.

The CL predictions for specimen S2 and S3 are presented in Figures 11 and 12, respectively, and shape predictions and CRAs are presented in Figures 13 and 14, respectively, yielding the same conclusions drawn from Figures 7 ~ 10, demonstrating the robustness of the proposed method over different specimens. Though the performance of the method for each specimen is noted slightly different, due to the stochasticity of delamination growth and also the initial ranges for those CL parameters, the method could cope with these uncertainties by online updating the CL model parameters.

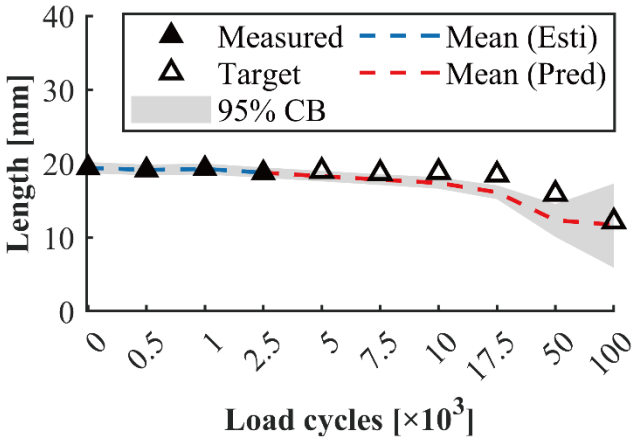

(a) 2500 load cycles, CL4, specimen S2

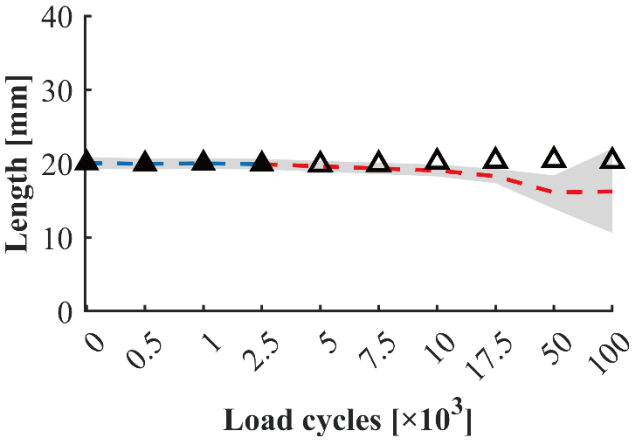

(b) 2500 load cycles, CL8, specimen S2

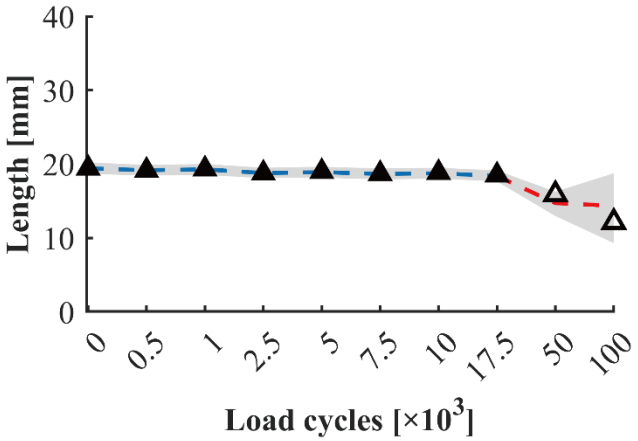

(c) 17500 load cycles, CL4, specimen S2

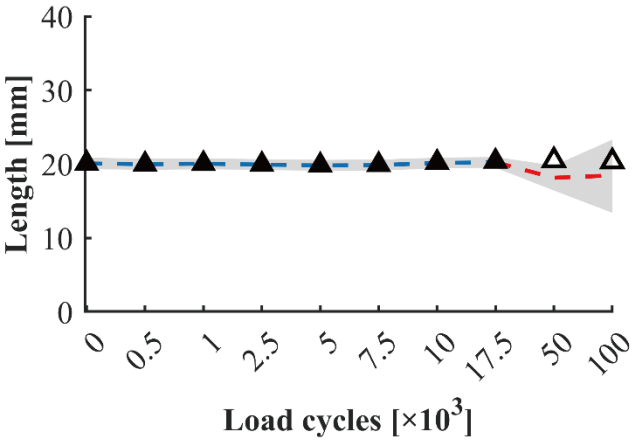

(d) 17500 load cycles, CL8, specimen S2

Figure 11 Predictions for two *x*-direction control lengths with the estimates at two selected load cycles for specimen S2

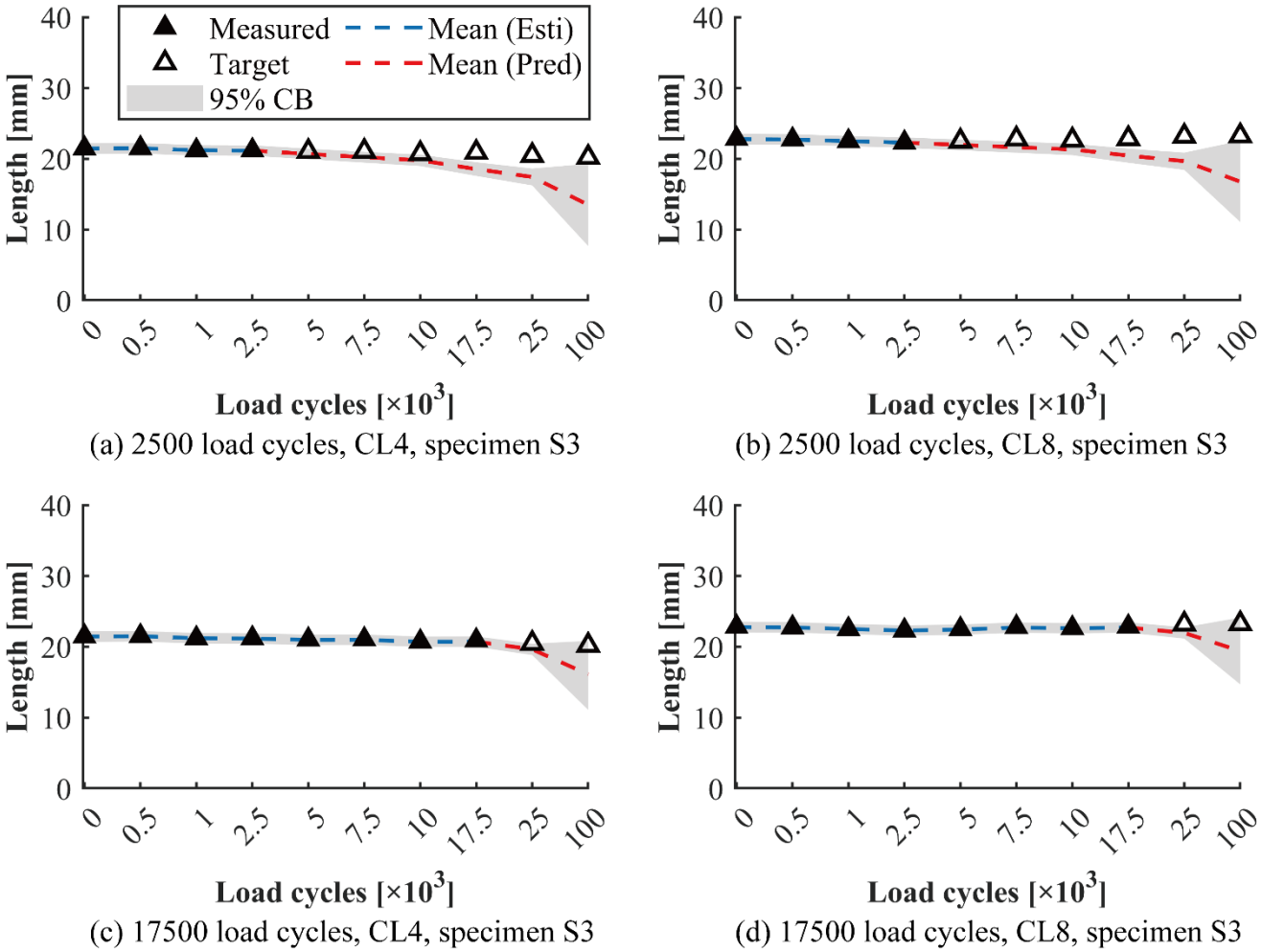

(a) 2500 load cycles, CL4, specimen S3

(b) 2500 load cycles, CL8, specimen S3

(c) 17500 load cycles, CL4, specimen S3

(d) 17500 load cycles, CL8, specimen S3

Figure 12 Predictions for two *x*-direction control lengths with the estimates at two selected load cycles for specimen S3

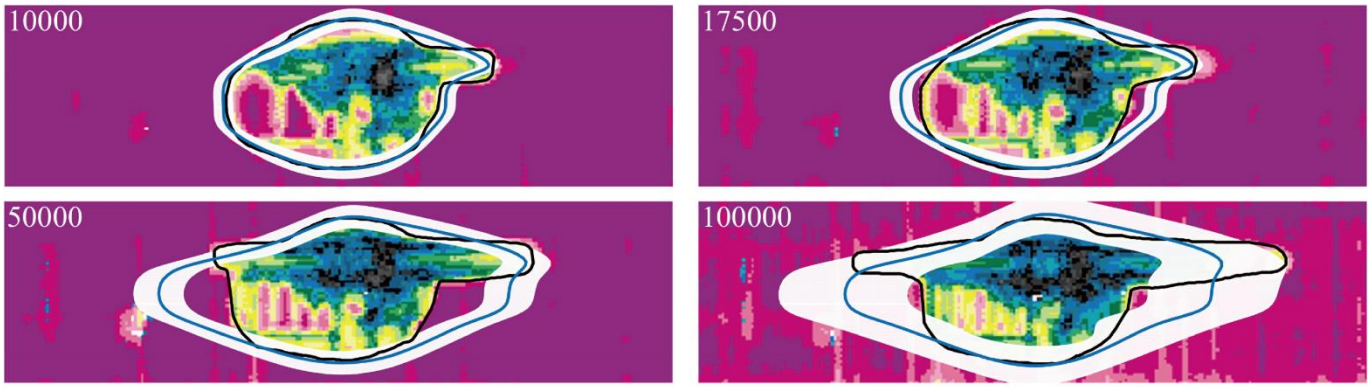

(a) Prediction based on the parameter estimates at 2500 load cycles, specimen S2

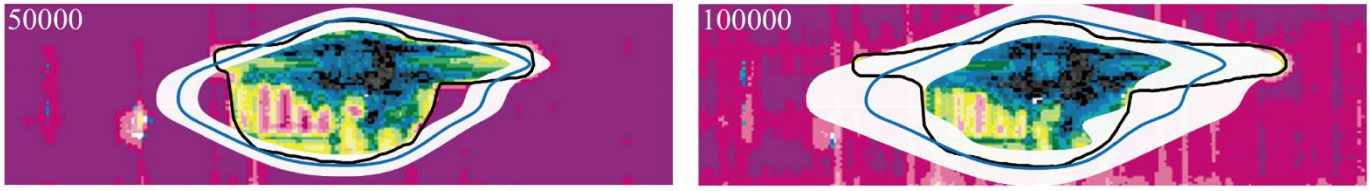

(b) Prediction based on the parameter estimates at 17500 load cycles, specimen S2

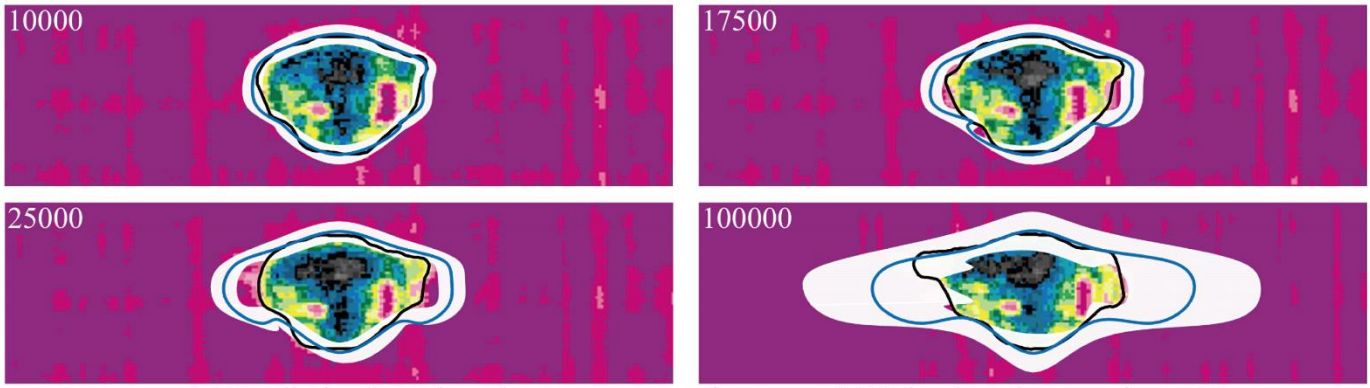

(c) Prediction based on the parameter estimates at 2500 load cycles, specimen S3

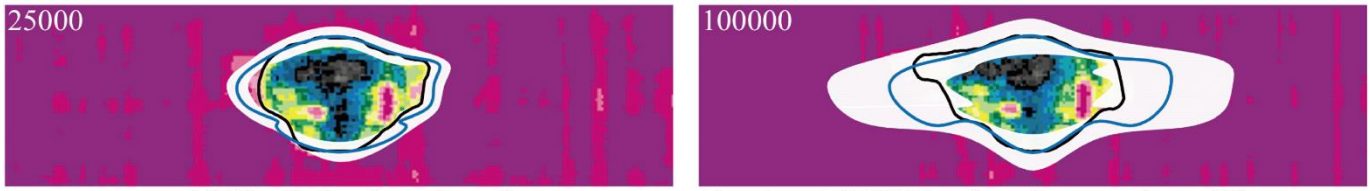

(d) Prediction based on the parameter estimates at 17500 load cycles, specimen S3

Figure 13 Shape predictions for specimens S2 and S3

Note: the load cycles at which the future shape is predicted are in the left-top corner. The black curve, blue curve, and white area are the target shape, the predicted shape, and its 95% CBs, respectively.

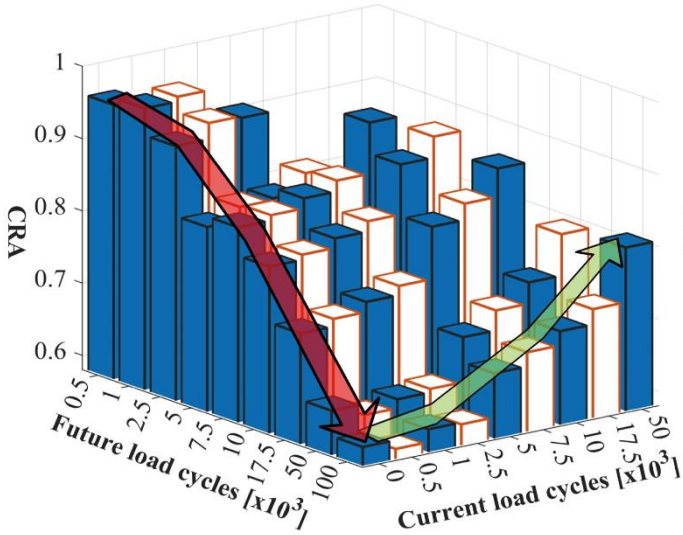

(a) Specimen S2

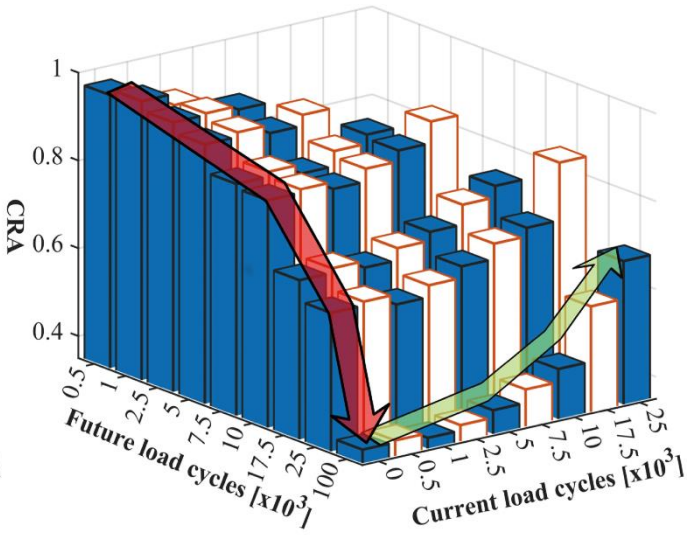

(b) Specimen S3

Figure 14 Cumulative relative accuracies (CRAs) of shape predictions for specimens S2 and S3

4. Conclusions

This paper has developed a novel particle filter-based delamination shape prediction method for composites by taking the delamination shape as a damage state for damage prognosis. By artificially defining a number of control lengths (CLs) to discretize the delamination contour, the shape prediction problem can be simplified into the predictions of these CLs, whose efficiency has been demonstrated with reference to experimental tests of fatigue delamination growth in composite panels with ultrasonics C-scan monitoring during the entire run-to-failure process. This method has been proven robust over different specimens, as it can consider the uncertainties of damage evolution by online updating the CL model parameters.

To move towards a more practical application for delamination shape prediction, one may consider four potential development paths for this research.

- Sufficient experimental or in-field delamination images during the run-to-failure process are required in this study to train the initial ranges in PF, which, however, may not always be feasible due to unconceivable costs. Thus, one may resort to simulated data, e.g., from a finite element model, for the definition of the initial ranges. The uncertainties arising from the difference between the numerical and experimental delamination growths can then be automatically taken care of by the adaptation capabilities of PF.
- In case even numerically generated data are not available, one may, for example, fit the model parameters by assuming no delamination growth during the fatigue test and then create sufficiently wide initial ranges for the parameters in PF implementation, probably at the expense of slower convergence and larger uncertainty intervals at early steps, thus calling for some PF modifications for fast convergence.
- Provided that the adaptability of a quadratic function may not be sufficient for other practical cases with too large uncertainties, involving, for example, more complex delamination shapes, delamination depth, etc., a more sophisticated surrogate model like Gaussian process or neural network could be implemented for building a more detailed damage evolution model.
- Given the difficulty of the online implementation of the Ultrasonic C-scan monitoring system, an online measurement system, e.g., guided wave, can be adopted for inferring the delamination shapes through a data-driven function mapping between the shape and measurements, finally yielding an online damage prognosis framework for industrial application.

Finally, the general idea discussed in this work, i.e., the simplification of a 2-dimensional prediction

problem into the predictions of some control points, can potentially contribute to the other applications, e.g., for the deformation estimate during the service life of a structure, which is left for the interested readers.

Appendix A1

Figures A.1, A.2, and A.3 present the images of the delamination and its contour at different load cycles from specimens S1, S2, and S3, respectively.

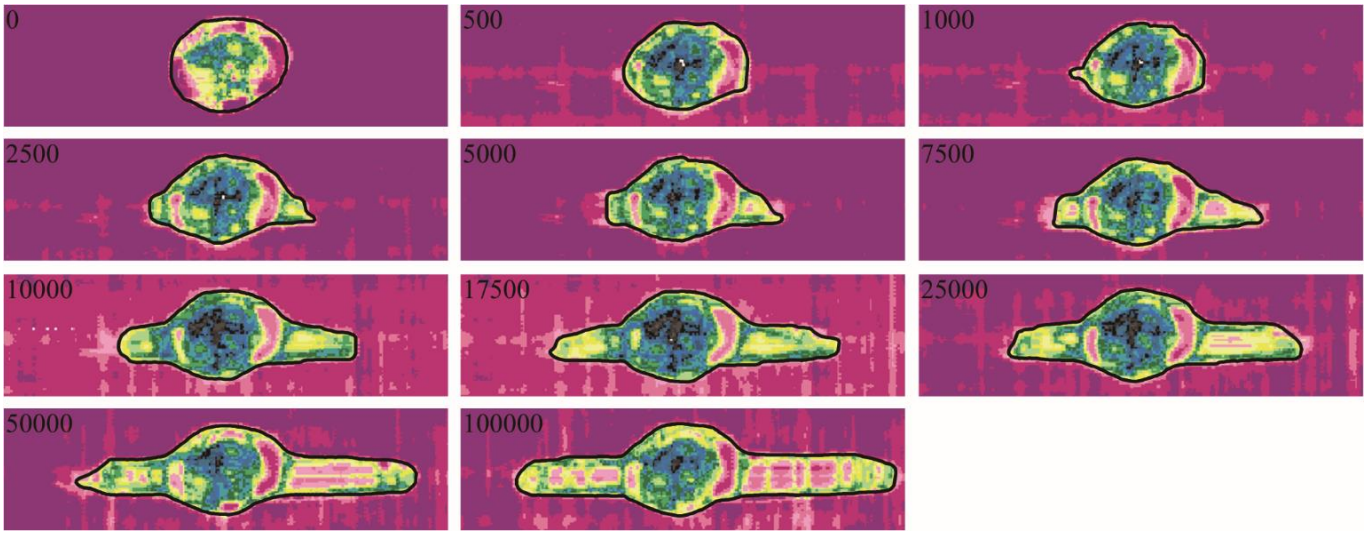

Figure A.1 Ultrasonic C-scan delamination images at different load cycles from specimen S1

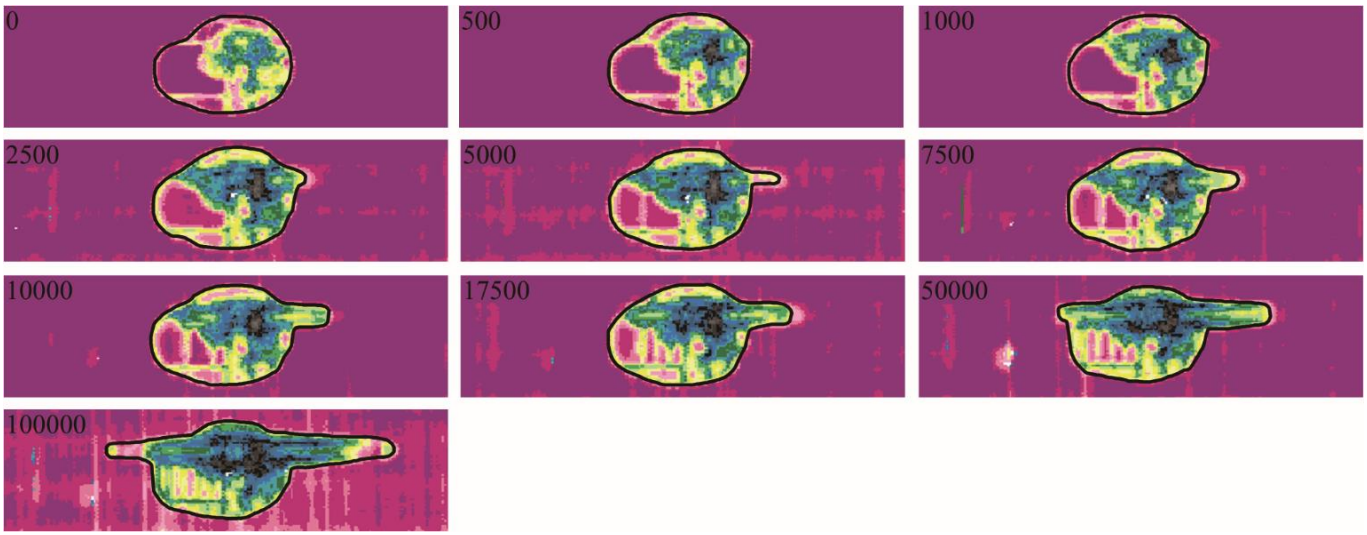

Figure A.2 Ultrasonic C-scan delamination images at different load cycles from specimen S2

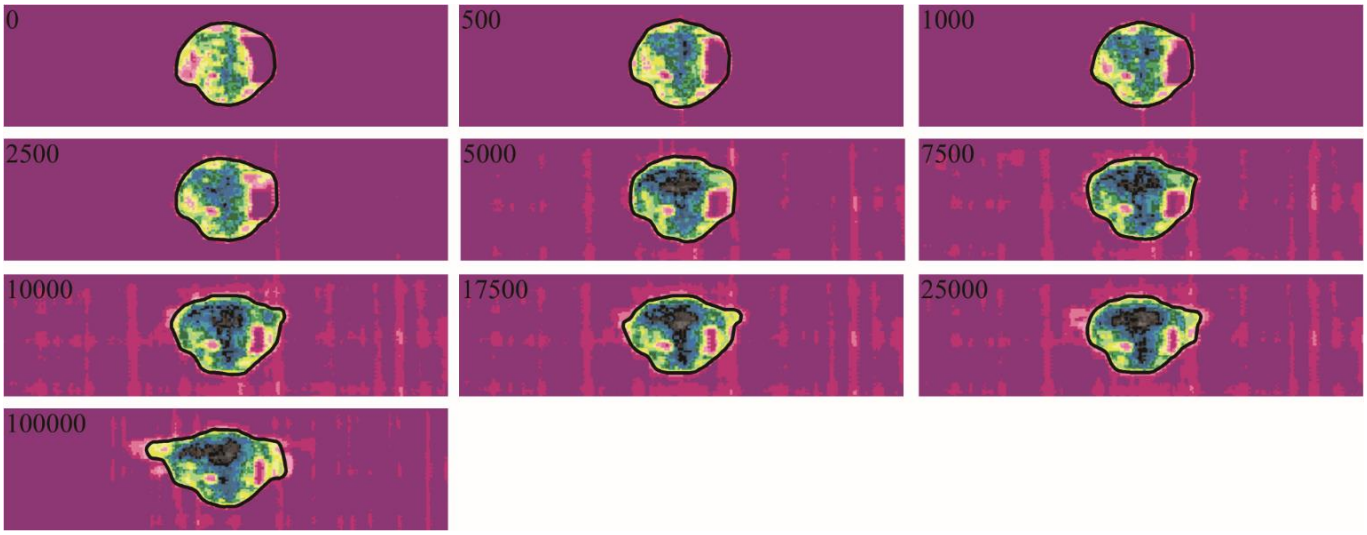

Figure A.3 Ultrasonic C-scan delamination images at different load cycles from specimen S3

Acknowledgments

This project has received funding from the European Union's Horizon 2020 research and innovation programme under the Marie Skłodowska-Curie grant agreement No. 859957. Also, the authors would like to thank the Institute of Polymers and Composites at Hamburg University of Technology (TUHH), for their collaborative support regarding the production of samples and the collection of monitoring data.

References

1. Chiachío M, Chiachío J, Sankararaman S, et al. A new algorithm for prognostics using Subset Simulation. *Reliability Engineering & System Safety* 2017; 168: 189-199. DOI: https://doi.org/10.1016/j.ress.2017.05.042.
2. Corbetta M, Sbarufatti C, Giglio M, et al. A Bayesian framework for fatigue life prediction of composite laminates under co-existing matrix cracks and delamination. *Composite Structures* 2018; 187: 58-70. DOI: https://doi.org/10.1016/j.compstruct.2017.12.035.
3. Cristiani D, Sbarufatti C and Giglio M. Damage diagnosis and prognosis in composite double cantilever beam coupons by particle filtering and surrogate modelling. *Structural Health Monitoring* 2020: 1475921720960067. DOI: 10.1177/1475921720960067.
4. Datta S, Neerukatti RK and Chattopadhyay A. Buckypaper embedded self-sensing composite for real-time fatigue damage diagnosis and prognosis. *Carbon* 2018; 139: 353-360. DOI: https://doi.org/10.1016/j.carbon.2018.06.059.
5. Chiachío J, Chiachío M, Sankararaman S, et al. Condition-based prediction of time-dependent reliability in composites. *Reliability Engineering & System Safety* 2015; 142: 134-147. DOI: https://doi.org/10.1016/j.ress.2015.04.018.
6. Tao C, Zhang C, Ji H, et al. Application of neural network to model stiffness degradation for composite laminates under cyclic loadings. *Composites Science and Technology* 2021; 203: 108573.
7. Eleftheroglou N, Zarouchas D and Benedictus R. An adaptive probabilistic data-driven methodology for prognosis of the fatigue life of composite structures. *Composite Structures* 2020; 245: 112386. DOI: https://doi.org/10.1016/j.compstruct.2020.112386.
8. Loutas T, Eleftheroglou N and Zarouchas D. A data-driven probabilistic framework towards the in-situ prognostics of fatigue life of composites based on acoustic emission data. *Composite Structures* 2017;

161: 522-529. DOI: https://doi.org/10.1016/j.compstruct.2016.10.109.
9. Peng Y, Dong M and Zuo MJ. Current status of machine prognostics in condition-based maintenance: a review. *The International Journal of Advanced Manufacturing Technology* 2010; 50: 297-313.
10. Liao L and Köttig F. Review of Hybrid Prognostics Approaches for Remaining Useful Life Prediction of Engineered Systems, and an Application to Battery Life Prediction. *IEEE Transactions on Reliability* 2014; 63: 191-207. DOI: 10.1109/TR.2014.2299152.
11. Lei Y, Li N, Guo L, et al. Machinery health prognostics: A systematic review from data acquisition to RUL prediction. *Mechanical Systems and Signal Processing* 2018; 104: 799-834. DOI: https://doi.org/10.1016/j.ymssp.2017.11.016.
12. Lopez I and Sarigul-Klijn N. A review of uncertainty in flight vehicle structural damage monitoring, diagnosis and control: Challenges and opportunities. *Progress in Aerospace Sciences* 2010; 46: 247-273. DOI: https://doi.org/10.1016/j.paerosci.2010.03.003.
13. Baraldi P, Mangili F and Zio E. Investigation of uncertainty treatment capability of model-based and data-driven prognostic methods using simulated data. *Reliability Engineering & System Safety* 2013; 112: 94-108. DOI: https://doi.org/10.1016/j.ress.2012.12.004.
14. Chen J, Yuan S and Wang H. On-line updating Gaussian process measurement model for crack prognosis using the particle filter. *Mechanical Systems and Signal Processing* 2020; 140: 106646. DOI: https://doi.org/10.1016/j.ymssp.2020.106646.
15. Li T, Sbarufatti C, Cadini F, et al. Particle filter-based hybrid damage prognosis considering measurement bias. *Structural Control and Health Monitoring* 2021; n/a: e2914. https://doi.org/10.1002/stc.2914. DOI: https://doi.org/10.1002/stc.2914.
16. Corbetta M, Sbarufatti C, Giglio M, et al. Optimization of nonlinear, non-Gaussian Bayesian filtering for diagnosis and prognosis of monotonic degradation processes. *Mechanical Systems and Signal Processing* 2018; 104: 305-322. DOI: https://doi.org/10.1016/j.ymssp.2017.11.012.
17. Jouin M, Gouriveau R, Hissel D, et al. Particle filter-based prognostics: Review, discussion and perspectives. *Mechanical Systems and Signal Processing* 2016; 72-73: 2-31. DOI: https://doi.org/10.1016/j.ymssp.2015.11.008.
18. Abhinav Saxena KG, Cecilia C. Larrosa, and Fu-Kuo Chang. CFRP Composites Data Set. NASA Ames Prognostics Data Repository (http://ti.arc.nasa.gov/project/prognostic-data-repository), NASA Ames Research Center, Moffett Field, CA.
19. Tian Z, Lingyu Y, Leckey C, et al. Guided wave imaging for detection and evaluation of impact-induced delamination in composites. *Smart Materials and Structures* 2015; 24: 105019. DOI: 10.1088/0964-1726/24/10/105019.
20. Li X, Kupski J, Teixeira De Freitas S, et al. Unfolding the early fatigue damage process for CFRP cross-ply laminates. *International Journal of Fatigue* 2020; 140: 105820. DOI: https://doi.org/10.1016/j.ijfatigue.2020.105820.
21. Tibaduiza DA, Torres-Arredondo MA, Mujica LE, et al. A study of two unsupervised data driven statistical methodologies for detecting and classifying damages in structural health monitoring. *Mechanical Systems and Signal Processing* 2013; 41: 467-484. DOI: https://doi.org/10.1016/j.ymssp.2013.05.020.
22. Cadini F, Sbarufatti C, Corbetta M, et al. Particle filtering-based adaptive training of neural networks for real-time structural damage diagnosis and prognosis. *Structural Control and Health Monitoring* 2019; 26. DOI: 10.1002/stc.2451.
23. Sbarufatti C, Corbetta M, Giglio M, et al. Adaptive prognosis of lithium-ion batteries based on the combination of particle filters and radial basis function neural networks. *Journal of Power Sources* 2017; 344: 128-140. DOI: https://doi.org/10.1016/j.jpowsour.2017.01.105.
24. Arulampalam MS, Maskell S, Gordon N, et al. A tutorial on particle filters for online nonlinear/non-Gaussian Bayesian tracking. *IEEE Transactions on Signal Processing* 2002; 50: 174-188. DOI:

10.1109/78.978374.
25. Chen Z. Bayesian Filtering: From Kalman Filters to Particle Filters, and Beyond. *Statistics* 2003; 182. DOI: 10.1080/02331880309257.
26. Saxena A, Celaya J, Balaban E, et al. Metrics for evaluating performance of prognostic techniques. In: *2008 International Conference on Prognostics and Health Management* 6-9 Oct. 2008 2008, pp.1-17.
27. Davies KB and Feddersen CE. Evaluation of fatigue-crack growth rates by polynomial curve fitting. *International Journal of Fracture* 1973; 9: 116-118. DOI: 10.1007/BF00035965.
28. Zhang Y, Vassilopoulos AP and Keller T. Fracture of adhesively-bonded pultruded GFRP joints under constant amplitude fatigue loading. *International Journal of Fatigue* 2010; 32: 979-987.
29. Liu J and West M. Combined parameter and state estimation in simulation-based filtering. *Sequential Monte Carlo methods in practice*. Springer, 2001, pp.197-223.
30. Chatzi EN and Smyth AW. The unscented Kalman filter and particle filter methods for nonlinear structural system identification with non-collocated heterogeneous sensing. *Structural Control & Health Monitoring* 2009; 16: 99-123. DOI: https://doi.org/10.1002/stc.290.

Table 1 Sampling importance resampling particle filter for one CL

Initialization: draw N_p particles $\{\boldsymbol{\theta}_{l,0}^i: i = 1,2,\dots,N_p\}$ from the initial distribution $p(\boldsymbol{\theta}_{l,0})$

For k=1, 2, …,

Prediction in PF: draw N_p particles $\{\boldsymbol{\theta}_{l,k}^i: i = 1,2,\dots,N_p\}$ by $\boldsymbol{\theta}_{l,k}^i \sim p(\boldsymbol{\theta}_{l,k}|\boldsymbol{\theta}_{l,k-1}^i)$

Weight update: calculate the weight w_k^i by $w_k^i \propto p(z_k|\boldsymbol{\theta}_{l,k}^i)$, and assign its normalized form $\widetilde{w}_k^i$ to each particle $\boldsymbol{\theta}_{l,k}^i$

Resample for $\{\boldsymbol{\theta}_{l,k}^i: i = 1,2,\dots,N\}$ using the particle weights $\{\widetilde{w}_k^i: i = 1,2,\dots,N\}$

Approximate the estimate $\widehat{\boldsymbol{\theta}}_{l,k}$ as $\widehat{\boldsymbol{\theta}}_{l,k} = \frac{1}{N}\sum_{i=1}^{N} \boldsymbol{\theta}_{l,k}^i$

End

Table 2 Calculation of future *l*-th control length

For $i = 1 : N_p$

For $j = 1, 2, 3, \ldots$

Calculate future $z_{l,k}^{i,j}$ as $z_{l,k}^{i,j} = f_l\left(N_{k+j}, \boldsymbol{\theta}_{l,k}^{i}\right)$

End

End

Table 3 Mechanical and manufacturing parameters of the

Type	Parameter	Value	Units	Description
Mechanical	E_m	*3.52*	*GPa*	*Matrix stiffness*
	ν_m	*0,35*	--	*Poisson's ratio of the matrix*
	E_{fx}	*240*	*GPa*	*X-axis laminate stiffness*
	E_{fy}	*28*	*GPa*	*Y-axis laminate stiffness*
	σ_{fx}	*1160*	*MPa*	*X-axis failure tension*
Manufacturing	v_f	*0.65*	--	*Fiber volume fraction*
	ρ_f	*1770*	Kg/m^3	*Fiber density*

Table 4 Particle filter parameters for the l-th control length

Number of particles N_p	STD in likelihood function σ_y	Kernel smoothing parameter h
6000	8	0.2
Initial ranges for $\{p_{1,l}, p_{2,l}, p_{3,l}\}$		
$p_{1,l}$	$p_{2,l}$	$p_{3,l}$
$U(m_{1,l} - r_{1,l}, m_{1,l} + r_{1,l})$	$U(m_{2,l} - r_{2,l}, m_{2,l} + r_{2,l})$	$U(m_{3,l} - r_{3,l}, m_{3,l} + r_{3,l})$
Distributions of process noises $\{\omega_{1,l}, \omega_{2,l}, \omega_{3,l}\}$ for $\{p_{1,l}, p_{2,l}, p_{3,l}\}$		
$\omega_{1,l}$	$\omega_{2,l}$	$\omega_{3,l}$
$\mathcal{N}(0, (2 \times 10^{-11})^2)$	$\mathcal{N}(0, (2 \times 10^{-6})^2)$	$\mathcal{N}(0, 20^2)$

Note: (a) $\{m_1, m_2, m_3\}$ and $\{r_1, r_2, r_3\}$ are the PF parameters for defining the initial ranges; (b) the terms $U(\cdot)$ and $\mathcal{N}(\cdot)$ indicate uniform distribution and Gaussian probability density function, respectively.

Table 5 Four groups of control lengths

Group	Direction	Control length (CL)	$\{m_1, m_2, m_3\}$	$\{r_1, r_2, r_3\}$
1	x	1, 2, 7 ,8	$\{3.09 \times 10^{-9}, -8.85 \times 10^{-4}, 417\}$-	$\{8 \times 10^{-9}, 8 \times 10^{-4}, 80\}$
2	x	3, 4, 5, 6	$\{0.88 \times 10^{-9}, -3.86 \times 10^{-4}, 404\}$	$\{8 \times 10^{-9}, 8 \times 10^{-4}, 80\}$
3	y	9, 10, 13, 14	$\{-0.16 \times 10^{-9}, -0.25 \times 10^{-4}, 73\}$	$\{2 \times 10^{-9}, 2 \times 10^{-4}, 40\}$
4	y	11, 12	$\{-2.57 \times 10^{-9}, 3.13 \times 10^{-4}, 37\}$	$\{2 \times 10^{-9}, 2 \times 10^{-4}, 40\}$